

# Symmetry Adapted Analysis of Screw Dislocation: Electronic Structure and Carrier Recombination Mechanisms in GaN

Yuncheng Xie,<sup>1, 2, \*</sup> Haozhe Shi,<sup>1, 2, \*</sup> Menglin Huang,<sup>2, 3</sup> Weibin Chu,<sup>1, 2</sup> Shiyu Chen,<sup>2, 3</sup> and Xin-Gao Gong<sup>1, 2</sup>

<sup>1</sup>*Department of Physics, Fudan University, Shanghai 200433, China*

<sup>2</sup>*Key Laboratory of Computational Physical Sciences (Ministry of Education),*

*State Key Laboratory of Surface Physics, Fudan University, Shanghai 200433, China*

<sup>3</sup>*College of Integrated Circuits and Micro-Nano Electronics, Fudan University, Shanghai 200433, China*

(Dated: January 28, 2026)

As fundamental one-dimensional defects, screw dislocations profoundly reshape the energy landscape and carrier dynamics of crystalline materials. By restoring the exact algebra of the screw dislocation group, we unveil the latent symmetry constraints that govern the electronic structure, providing a more rigorous physical picture than the conventional treatments. When applied to GaN, the method yields a band-connectivity constraint and rigorous dipole selection rules for polarization-resolved transitions. Combined with computed Hamiltonian matrix, the approach gives symmetry-filtered radiative and dielectric calculations and reveals a piezoelectrical effect at the dislocation core that strongly suppresses radiative recombination. The pronounced dominance of non-radiative capture over radiative recombination highlights the detrimental impact of screw dislocations on the luminous efficiency of GaN, providing a theoretical foundation for optimizing dislocation-limited optoelectronic devices.

## I. INTRODUCTION

Screw dislocations are prevalent in semiconductor materials and can significantly affect material properties, particularly electronic processes such as radiative and nonradiative carrier recombination [1]. Understanding these mechanisms is important for the design of next-generation semiconductor devices [2–7].

Since a screw dislocation breaks the translational symmetry perpendicular to the dislocation axis, the conventional Bloch theorem no longer directly applies. Therefore previous studies have typically employed large supercells and performed density functional theory (DFT) calculation [8–11]. While the supercell method remains the standard for modeling dislocation geometries, traditional DFT treatments often view these large ensembles as mere disordered clusters, thereby failing to exploit the underlying screw symmetry inherent in the structure. Consequently, the rich physical information remains locked within an unnecessarily large and opaque Hamiltonian. This paper presents a framework that, while still utilizing the supercell geometry, explicitly recovers and leverages this hidden symmetry to block-diagonalize the electronic structure and unveil novel mathematical features [12, 13].

In this paper, we first present a rigorous theoretical analysis of the symmetry properties inherent to screw dislocations. This framework establishes a symmetry-adapted basis that allows the Hamiltonian to be block-diagonalized, with each block corresponding to a specific irreducible representation. Consequently, the total band structure is resolved into independent components labeled by these representations. Leveraging this decomposition, we reveal hidden interconnections between bands

originating from different symmetry channels. Beyond the electronic structure, we derive the dipole selection rules for polarization-resolved optical transitions. These rules facilitate the calculation of the radiative recombination coefficient, which is subsequently compared with its non-radiative counterpart. Our results provide critical insights and theoretical guidance for future experimental investigations into the optoelectronic properties of dislocations.

## II. SYMMETRY ADAPTED BASIS

In this section we develop a concise, self-contained theoretical framework for exploiting the  $n$ -fold screw symmetry that characterizes the systems studied in this work. We begin by constructing symmetry-adapted basis functions using the plane-wave approach. Due to the limitations of this method for screw-symmetric systems, we then introduce a localized atomic orbital framework. This construction yields basis functions that, as eigenstates of the screw operator, can effectively give a block-diagonalized Hamiltonian.

For generality we consider a  $n$ -fold screw operation that rotates by  $2\pi/n$  about the  $z$ -axis and translates by  $mc/n$  along  $z$ . So a screw symmetry is characterized by the rotation index  $m$  and translation index  $n$ .

### A. Screw operator and its representations

Let  $S$  denote the  $n$ -fold screw operator acting on spatial coordinates by

$$S : (x, y, z) \mapsto (x \cos \theta - y \sin \theta, x \sin \theta + y \cos \theta, z + mc/n), \quad (1)$$

\* These authors are co-first authors and contributed equally to this work.

where  $\theta = 2\pi/n$ . The Hamiltonian  $H$  of the crystal commutes with  $S$  in the idealized symmetry-preserving model, i.e.  $[H, S] = 0$ . For Bloch states labeled by the crystal momentum  $k_z$  along the  $z$ -axis the eigenvalues  $\lambda$  of  $S$  satisfy

$$\lambda^n = e^{ik_z mc}. \quad (2)$$

It is convenient to parametrize the  $n$  branches by an integer index  $\mu \in \{0, 1, \dots, n-1\}$ :

$$\lambda_\mu(k_z) = e^{i(k_z \frac{mc}{n} + \mu \frac{2\pi}{n})}. \quad (3)$$

### B. Plane-wave expansion

Consider the standard plane-wave ansatz used in supercell electronic-structure calculations,

$$\psi_{k_z, \mathbf{G}_{\parallel}, \ell}(\mathbf{r}) = e^{ik_z z} e^{i\mathbf{G}_{\parallel} \cdot \mathbf{r}_{\parallel}}, \quad (4)$$

where  $\mathbf{r}_{\parallel} = (x, y)$  and  $\mathbf{G}_{\parallel}$  is an in-plane reciprocal-lattice vector (set by the supercell). To construct eigenstates of symmetry operator one must form linear combinations of plane waves whose in-plane wavevectors are related by the  $C_n$  rotation. For each orbit of  $n$  rotated wavevectors  $\{\mathbf{G}_{\parallel}, R_z(\theta)\mathbf{G}_{\parallel}, \dots\}$  one can form symmetry-adapted linear combinations that transform according to the representations in (3),

$$\phi_{\mathbf{G}_{\parallel}, l, \mu}(\mathbf{r}) = e^{ik_z z} \sum_{j=0}^{n-1} \left[ e^{i(\mu-l) \frac{2\pi}{n}} \right]^j e^{i\mathbf{G}_j \cdot (x, y)} e^{i\mathbf{G}_l z} \quad (5)$$

where  $\mathbf{G}_j$  are the rotated  $\mathbf{G}_{\parallel}$  vectors for  $j$  times and  $\mathbf{G}_l$  are the reciprocal lattice vectors along the screw axis ( $z$ -direction) associated with the index  $l$ .

While the plane-wave method is effective for standard electronic structure calculations, it poses significant challenges for the explicit symmetry analysis pursued in this work. Specifically, the symmetry-based decomposition requires the construction and manipulation of the Hamiltonian matrix. Given the large number of plane waves (determined by a fine in-plane  $\mathbf{G}_{\parallel}$  grid), the resulting Hamiltonian matrix becomes exceedingly large. This high dimensionality makes the subsequent block-diagonalization and analytical interpretation computationally prohibitive.

These considerations motivate the construction of a more compact basis set that remains adapted to the action of  $S$ . Localized atomic orbitals, when combined with Bloch sums along  $z$  and appropriate screw-symmetrization, provide an ideal framework for this purpose, offering a much more manageable matrix dimension for symmetry analysis.

### C. Localized atomic orbitals

We assume a set of localized orbitals  $\{|R, \alpha\rangle\}$  centered at atomic sites  $R = (x_R, y_R, z_R)$ , where  $\alpha$  labels orbital

type (e.g. site index within the projected unit cell and orbital angular momentum). The atomic positions are invariant under translation by  $c$  along  $z$  and under the screw  $S$  (in the sense that for each site  $R$  the site  $SR$  is also present). Because translation by  $c$  is a symmetry we may form Bloch sums along  $z$ :

$$|R, \alpha; k_z\rangle \equiv \frac{1}{\sqrt{N_z}} \sum_{n \in \mathbb{Z}} e^{ik_z z_{R,n}} |R + nc\hat{z}, \alpha\rangle, \quad (6)$$

where  $z_{R,n} = z_R + nc$  and  $N_z$  is the number of cells along  $z$  used for normalization. These states carry the Bloch phase  $e^{ik_z c}$  under  $T_z(c)$  and remain localized in the projected  $xy$ -plane.

Sites in a given  $C_n$  orbit can be labeled by a representative index  $p$  and an internal index  $j \in \{0, 1, \dots, n-1\}$  such that  $R_{p,j} = S^j R_{p,0}$ . Denote the corresponding Bloch-summed orbitals by  $|p, j; \alpha; k_z\rangle$ .

We now form screw-symmetry-adapted linear combinations with localized atomic orbital symmetrization. For each orbit  $p$ , orbital label  $\alpha$ , Bloch momentum  $k_z$  and representation index  $\mu$  define

$$|\chi_{p, \alpha, k_z, \mu}\rangle \equiv \frac{1}{\sqrt{n}} \sum_{j=0}^{n-1} e^{-ij\mu \frac{2\pi}{n}} U_j^{(\alpha)} |p, j; \alpha; k_z\rangle, \quad (7)$$

where  $U_j^{(\alpha)}$  denotes the action of the planar rotation  $R_z(j2\pi/n)$  on the orbital degrees of freedom (for scalar  $s$  orbitals  $U_j^{(\alpha)} = 1$ ). The coefficients  $e^{-ij\mu \frac{2\pi}{n}}$  implement projection onto the one-dimensional representation labeled by  $\mu$ .

### D. Proof: $|\chi_{p, \alpha, k_z, \mu}\rangle$ is the eigenstate of $S$

To validate (7) is actually the eigenstate of screw operator  $S$ , we act with  $S$  on (7). Using the geometric action  $SR_{p,j} = R_{p,j+1}$  and the fact that  $z$ -coordinates obey  $z_{p,j+1} = z_{p,j} + \frac{mc}{n}$ , together with the rotational action  $SU_j^{(\alpha)} = U_{j+1}^{(\alpha)}$ , one finds

$$\begin{aligned} S|\chi_{p, \alpha, k_z, \mu}\rangle &= \frac{1}{\sqrt{n}} \sum_{j=0}^{n-1} e^{-ij\mu \frac{2\pi}{n}} S U_j^{(\alpha)} |p, j; \alpha; k_z\rangle \\ &= \frac{1}{\sqrt{n}} \sum_{j=0}^{n-1} e^{-ij\mu \frac{2\pi}{n}} U_{j+1}^{(\alpha)} e^{ik_z \frac{mc}{n}} |p, j+1; \alpha; k_z\rangle \\ &= e^{ik_z \frac{mc}{n}} e^{i\mu \frac{2\pi}{n}} |\chi_{p, \alpha, k_z, \mu}\rangle. \end{aligned} \quad (8)$$

Therefore  $|\chi_{p, \alpha, k_z, \mu}\rangle$  is an eigenstate of  $S$  with eigenvalue  $\lambda_\mu(k_z)$  given in (3). The key ingredients are the explicit Bloch factors in (6) that use the true atomic  $z$ -coordinates and the  $C_n$  projection phases  $e^{-ij\mu \frac{2\pi}{n}}$ .

### E. Block-diagonalization of the Hamiltonian

Since  $|\chi_{p, \alpha, k_z, \mu}\rangle$  is an eigenstate of the screw operator  $S$ , the commutativity  $[H, S] = 0$  dictates that the

Hamiltonian  $H$  can be block-diagonalized in accordance with the principles of group theory. Consider the matrix element between two symmetry-adapted states with representation indices  $\mu$  and  $\mu'$ ,

$$H_{\mu\mu'} \equiv \langle \chi_{p,\alpha,k_z,\mu} | H | \chi_{q,\beta,k_z,\mu'} \rangle. \quad (9)$$

Because  $S$  commutes with  $H$  we can insert  $S^{-1}S$  adjacent to  $H$  and use that  $S|\chi_{\cdot,\mu}\rangle = \lambda_{\mu}|\chi_{\cdot,\mu}\rangle$  to obtain

$$H_{\mu\mu'} = \lambda_{\mu}^* \lambda_{\mu'} H_{\mu\mu'}. \quad (10)$$

Hence

$$(1 - \lambda_{\mu}^* \lambda_{\mu'}) H_{\mu\mu'} = 0. \quad (11)$$

If  $\lambda_{\mu} \neq \lambda_{\mu'}$  (which holds for  $\mu \neq \mu'$  for generic  $k_z$ ) we conclude  $H_{\mu\mu'} = 0$ . Thus matrix elements between different screw representations vanish and the Hamiltonian is block-diagonal in the basis  $\{|\chi_{p,\alpha,k_z,\mu}\rangle\}$ .

In practice, we can construct the projection operators to block-diagonalize the original Hamiltonian. Define the  $k$ -dependent projector onto the  $\mu$ -th screw representation by the standard discrete Fourier projector in the group algebra:

$$P_{\mu}(k) = \frac{1}{n} \sum_{j=0}^{n-1} \lambda_{\mu}(k)^{-j} \hat{S}^j, \quad (12)$$

where the eigenvalues  $\lambda_{\mu}$  are defined as (3) and for any state  $|\psi\rangle$  with  $\hat{S}|\psi\rangle = \lambda_{\mu}(k)|\psi\rangle$  the projector acts as  $P_{\mu}(k)|\psi\rangle = |\psi\rangle$ . Therefore the Hamiltonian decomposes as

$$\hat{H} = \sum_{\mu=0}^{n-1} P_{\mu}(k) \hat{H} P_{\mu}(k) = \bigoplus_{\mu=0}^{n-1} H_{\mu}(k). \quad (13)$$

Each block  $H_{\mu}(k) = P_{\mu}(k) \hat{H} P_{\mu}(k)$  acts only within the  $\mu$ -th symmetry subspace and may be diagonalized independently, yielding bands  $\epsilon_{n,\mu}(k_z)$  that are classified by the screw representation.

### III. ELECTRONIC STRUCTURE

#### A. Crystal structure and computational method

We employ the single 6-atom-ring full-core model [14, 15], a standard configuration in GaN screw dislocation calculations, as a test case for our study. The dislocation core is located at the center of a hexagonal GaN ring, characterized by a Burgers vector  $\mathbf{b} = [0001]c$ , where  $c$  denotes the structural repetition parameter along the  $z$ -direction. This configuration exhibits a  $6_2$  screw symmetry with respect to the dislocation center, which means the rotation index  $n = 6$  and translation index  $m = 2$ . Therefore, the generator of the screw symmetry is taken to be

$$\hat{S} = \{C_6 \mid c/3\}, \quad (14)$$

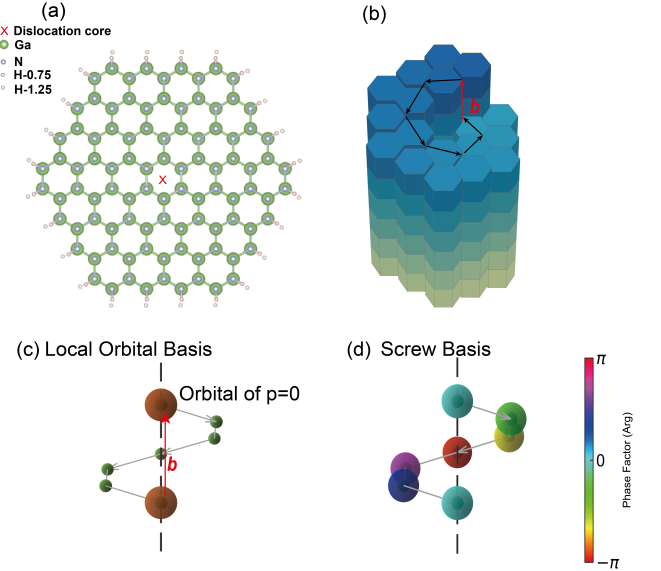


FIG. 1. Structural models of a screw-dislocation GaN nanowire. (a) Cross-sectional structure of the nanowire passivated by fractional H atoms. (b) Schematic illustration of the screw dislocation symmetry. (c, d) Schematic illustration of constructing screw-symmetry-adapted basis functions from localized atomic orbitals. The visualization depicts an  $s$ -orbital model at  $k_z = 0$  for the screw representation index  $\mu = 1$ .

where  $C_6$  is a rotation by  $2\pi/6$  about the axis and the translation component is  $c/3$  along the axis.

Given that the geometry of a screw dislocation inherently breaks translational symmetry, we adopt a quasi-one-dimensional GaN nanowire model. Vacuum layers are applied in the  $xy$ -plane to isolate the wire, and the lateral surfaces are passivated using pseudo-hydrogen atoms with fractional charges to eliminate dangling bond surface states.[8] To facilitate the symmetry-adapted analysis, the supercell is constructed to enclose complete symmetry orbits, ensuring that for any included atom, all its images generated by the screw operator are also present. The resulting atomic structure is illustrated in Fig. 1.

DFT calculations are performed using the ABACUS package to obtain the Hamiltonian in a localized atomic orbital representation [16–18]. This Hamiltonian is subsequently transformed and diagonalized within the symmetry-adapted subspaces. To ensure the accuracy of localized state bandgaps, we employed the HSE06 hybrid functional for calculations [19, 20].

#### B. Hamiltonian and Band structure

Theoretical analysis based on Eq. (13) indicates that the Hamiltonian for GaN ( $n = 6$ ) decomposes into six

distinct blocks. This block-diagonal structure is clearly visualized in the heatmap of the Hamiltonian within the localized-orbital basis (Fig. 2) once the projectors  $P_\mu(k)$  are applied. Independently diagonalizing each block yields the symmetry-resolved dispersion relations  $\{\epsilon_{n,\mu}(k)\}_n$  for  $\mu = 0, \dots, 5$ . The composite band structure, representing the union of these six sub-spectra, can be rendered as a color-coded plot that highlights the dominant  $\mu$ -character of each branch.

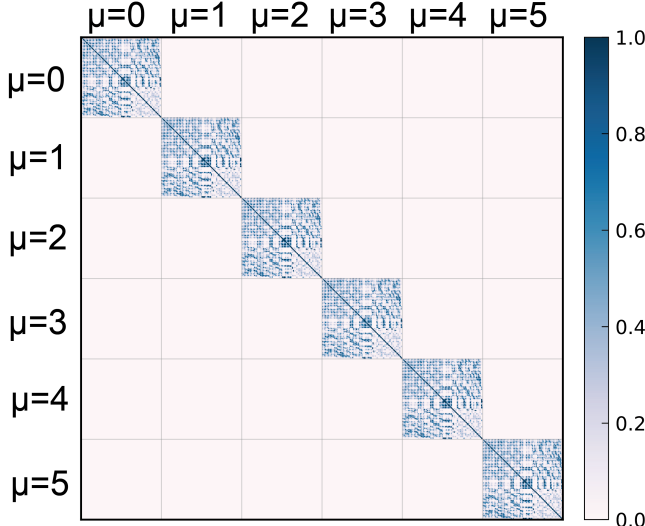


FIG. 2. Heatmap of the Hamiltonian matrix in the localized-orbital basis. The color represents the magnitude of the matrix elements. After transformation to the screw-symmetric basis the matrix decomposes into six independent blocks  $H_\mu(k)$ . This result presents the meaning of the symmetry-adapted basis.

Fig. 3 compares the band structures of ideal and screw-dislocated GaN nanowires. The pristine nanowire exhibits a band gap of 3.68 eV, in good agreement with experimental values (3.51 eV [21, 22]). Conversely, the introduction of a screw dislocation induces six distinct localized states and significantly reduces the band gap to 0.70 eV, consistent with prior findings [8]. Utilizing our symmetry-based analysis, we demonstrate that these localized states originate from the  $\mu = 0, 1$ , and  $5$  symmetry channels. Notably, the states flanking the Fermi level (labeled 3 and 4) are exclusively associated with the  $\mu = 0$  representation.

### C. Band connectivity and coupling chains

We now prove the band-flow relation that constrains how bands from different  $\mu$ -blocks connect across the Brillouin-zone boundary. Let the axial reciprocal-lattice vector be  $G = 2\pi/c$ . Under the translation  $k \rightarrow k + G$

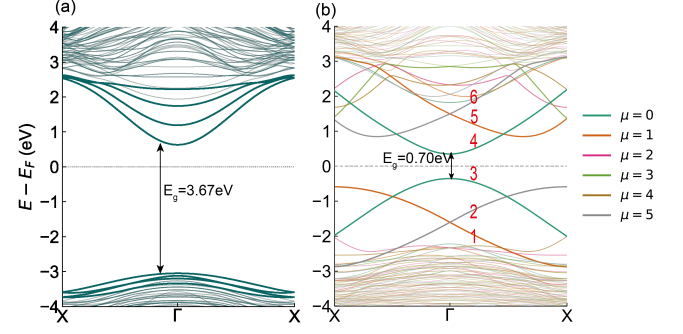


FIG. 3. Calculated band structures of GaN nanowires. (a) The ideal nanowire. (b) The screw-dislocated nanowire, where the dislocation-induced gap states are labeled from 1 to 6. The bands are color-coded according to their screw symmetry index  $\mu$ .

the phase in  $\lambda_\mu$  changes as

$$\begin{aligned} \lambda_\mu(k + G) &= \exp\left[i\left(\frac{(k + G)c}{3} + \frac{\pi\mu}{3}\right)\right] \\ &= \exp\left[i\left(\frac{kc}{3} + \frac{\pi\mu}{3} + \frac{2\pi}{3}\right)\right] \\ &= \exp\left[i\left(\frac{kc}{3} + \frac{\pi(\mu + 2)}{3}\right)\right] = \lambda_{\mu+2}(k), \end{aligned} \quad (15)$$

where the index  $\mu + 2$  is understood modulo six. Therefore the screw-eigenvalue of a state at  $(k + G)$  equals the screw-eigenvalue of a state in block  $\mu + 2$  at  $k$ . Energy bands are continuous functions of  $k$ , hence an eigenvalue branch originating in block  $\mu$  at wave vector  $k$  must connect to an eigenvalue branch in block  $\mu + 2$  upon translation by  $G$ . This establishes the band-flow rule

$$\Delta\mu = +2 \pmod{6} \quad \text{for } k \mapsto k + G. \quad (16)$$

Consequently, as the Fig. 4 shows, the six blocks split into two independent band-flow chains: the odd chain  $(1 \rightarrow 3 \rightarrow 5 \rightarrow 1)$  and the even chain  $(0 \rightarrow 2 \rightarrow 4 \rightarrow 0)$  (indices taken modulo six with an appropriate choice of origin). These coupling chains are mathematical constraints imposed by the screw symmetry and the associated phase accumulation; they are independent of microscopic Hamiltonian details and hence robust.

## IV. RADIATIVE RECOMBINATION

Having established the screw-symmetric decomposition of Hamiltonian and the symmetry-resolved bands  $\epsilon_{n,\mu}(k)$  in the preceding section, we now derive the optical selection rules and compute radiative observables for GaN systems with sixfold screw symmetry.

### A. Dipole operator and screw transformation

In the electric-dipole approximation the light-matter interaction is governed by the dipole operator  $\mathbf{d} = -e\mathbf{r}$ .

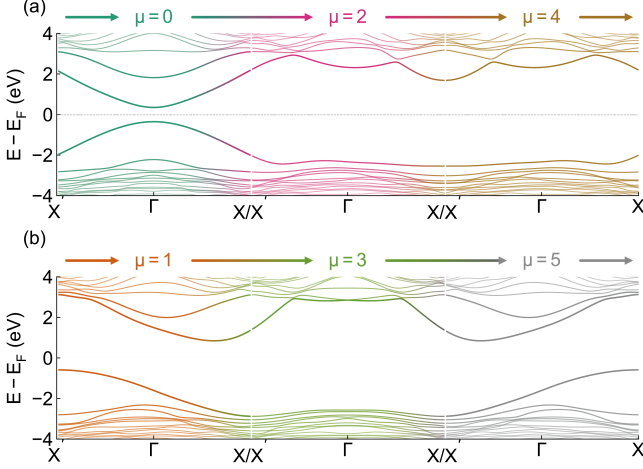


FIG. 4. Six blocks split into two independent band-flow chains: (a) the even chain ( $0 \rightarrow 2 \rightarrow 4 \rightarrow 0$ ); (b) the odd chain ( $1 \rightarrow 3 \rightarrow 5 \rightarrow 1$ ). This rule is the internal connection between bands from different blocks under screw symmetry.

Under the screw operator  $S = \{C_6 \mid c/3\}$  the spatial operators transform as

$$S \mathbf{r} S^{-1} = R_z(2\pi/6) \mathbf{r} + \tau, \quad S \mathbf{p} S^{-1} = R_z(2\pi/6) \mathbf{p}, \quad (17)$$

with  $\tau = (0, 0, c/3)$ . For transition matrix elements between distinct eigenstates the constant translation term does not contribute, so  $\mathbf{d}$  is treated as a rank-1 tensor under rotations.

It is convenient to decompose the dipole into spherical components  $d^{(m)}$  with  $m \in \{0, \pm 1\}$ :

$$d^{(0)} = -ez, \quad d^{(\pm 1)} = -\frac{e}{\sqrt{2}}(x \pm iy), \quad (18)$$

which transform under  $C_6$  as

$$S d^{(m)} S^{-1} = e^{i2\pi m/6} d^{(m)}. \quad (19)$$

## B. Selection rules

Let  $|\psi_{i,k}^{(\mu_i)}\rangle$  and  $|\psi_{f,k}^{(\mu_f)}\rangle$  be eigenstates of  $\hat{H}$  and  $S$  at the same axial wave vector  $k$ , with screw eigenvalues  $\lambda_{\mu_i}(k)$  and  $\lambda_{\mu_f}(k)$  defined in (3). Consider the dipole matrix element

$$M_{fi}^{(m)}(k) = \langle \psi_{f,k}^{(\mu_f)} | d^{(m)} | \psi_{i,k}^{(\mu_i)} \rangle. \quad (20)$$

Insert the identity  $S^{-1}S$  and use the transformation properties to obtain

$$\begin{aligned} M_{fi}^{(m)}(k) &= \langle \psi_{f,k}^{(\mu_f)} | S^{-1} S d^{(m)} S^{-1} S | \psi_{i,k}^{(\mu_i)} \rangle \\ &= \lambda_{\mu_f}(k)^* \lambda_{\mu_i}(k) e^{i2\pi m/6} M_{fi}^{(m)}(k). \end{aligned} \quad (21)$$

Nonzero matrix elements therefore require

$$\lambda_{\mu_f}(k)^* \lambda_{\mu_i}(k) e^{i2\pi m/6} = 1. \quad (22)$$

Using (3) the  $k$ -dependent phase cancels (photon momentum is neglected in the dipole approximation), yielding the compact selection rule

$$\Delta\mu \equiv \mu_f - \mu_i \equiv m \pmod{6}. \quad (23)$$

Thus axial polarization ( $m = 0$ ) connects states within the same block, while transverse circular polarizations connect blocks differing by  $\pm 1 \pmod{6}$ . This finding aligns with and further refines the general group-theoretic predictions, with the derived selection rules summarized in Table I.

TABLE I. Optical selection rules in screw-dislocated GaN.

Polarization $m$	Selection Rule	Interpretation
Axial ( $\parallel \hat{z}$ )	0 $\mu_f = \mu_i$	Intra-block only
Circular $\sigma^+$	+1 $\mu_f \equiv \mu_i + 1$	Screw momentum +1
Circular $\sigma^-$	-1 $\mu_f \equiv \mu_i - 1$	Screw momentum -1
Linear $E \perp \hat{z}$	$\pm 1 \mu_f \equiv \mu_i \pm 1$	Mixed $\pm 1$ channels

The calculated optical matrix elements in the screw basis are shown in Figs. 5(a) and (b), with the corresponding  $\Delta\mu$ -resolved imaginary parts of the dielectric function provided in (c) and (d). The results confirm our selection rules: transverse components ( $v_x, v_y$ ) mediate transitions restricted to  $\Delta\mu = \pm 1$ , whereas the axial component ( $v_z$ ) is confined to the  $\Delta\mu = 0$  channel due to its block-diagonal nature.

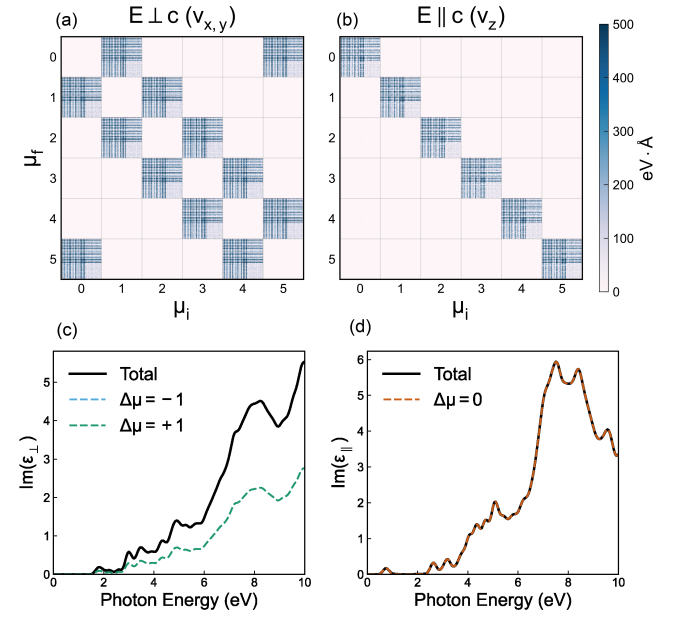


FIG. 5. Optical properties of screw-dislocated GaN nanowires. (a, b) Optical transition matrix elements in the screw basis for transverse (perpendicular to  $c$ ) and axial (parallel to  $c$ ) polarizations, respectively. (c, d) Imaginary parts of the dielectric function for the corresponding directions, showing the decomposition into different  $\Delta\mu$  channels.

### C. Radiative Recombination Rate

We calculate the band-to-band radiative recombination rate  $R_{\text{rad}}$  based on the theory of spontaneous emission within the electric dipole approximation.[23] For a system with refractive index  $n_r$ , the total spontaneous emission rate per unit volume at an injected carrier density  $n$  is given by:

$$R_{\text{rad}} = \frac{n_r e^2}{3\pi\epsilon_0 m_0^2 c^3 \hbar^2 V} \times \sum_k w_k \sum_{c \in \text{CB}} \sum_{v \in \text{VB}} f_c (1 - f_v) (E_{ck} - E_{vk}) |\mathbf{p}_{cv}(k)|^2, \quad (24)$$

where  $V$  is the effective volume determined by the nanowire cross-section,  $w_k$  are the  $k$ -point weights, and  $E_{ck}$  ( $E_{vk}$ ) are the eigenenergies of the conduction (valence) band states. The Fermi-Dirac occupation factors  $f_c$  and  $f_v$  are determined by the electron and hole quasi-Fermi levels,  $E_{Fn}$  and  $E_{Fp}$ , which are solved self-consistently to satisfy the charge neutrality condition  $n = \frac{1}{V} \sum_{k,c} f_c = \frac{1}{V} \sum_{k,v} (1 - f_v)$ .

Utilizing the screw Bloch basis, we decompose  $R_{\text{rad}}$  into symmetry channels defined by  $\Delta\mu = (\mu_c - \mu_v) \pmod{6}$ . The radiative coefficient is then given by  $B_{\text{rad}} = R_{\text{rad}}/n^2$ , which characterizes the optical polarization anisotropy.

Fig. 6 presents the computed radiative rates. We observe that in the GaN nanowire with a screw dislocation,  $R_{\text{rad}}$  is dominated by the  $\Delta\mu = 0$  channel, corresponding to states 3 and 4 at the  $\Gamma$  point at low carrier densities  $n$ . This corresponds to a photon energy of approximately 0.7 eV in the infrared region, which is predicted to exhibit polarization parallel to the screw dislocation line.

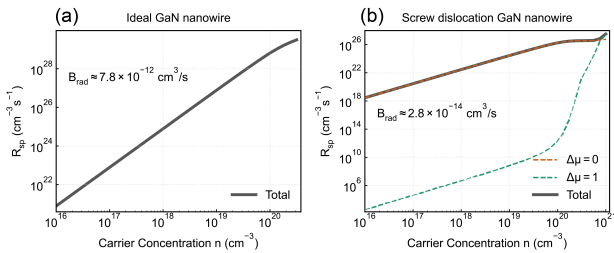


FIG. 6. Radiative recombination rate as a function of injected carrier density  $n$ . The decomposition into different  $\Delta\mu$  channels is indicated by dashed lines in different colors for (a) ideal GaN and (b) GaN with a screw dislocation. These comparison shows the existence of screw dislocation significantly suppresses the radiative ability of GaN.

Compared to the ideal GaN nanowire, the GaN nanowire containing screw dislocations exhibits a reduction in the radiative recombination rate by two to three orders of magnitude. To elucidate the microscopic origin of this phenomenon, we examine the electrostatic poten-

tial distribution and the atomic composition of the states that dominate radiative recombination.

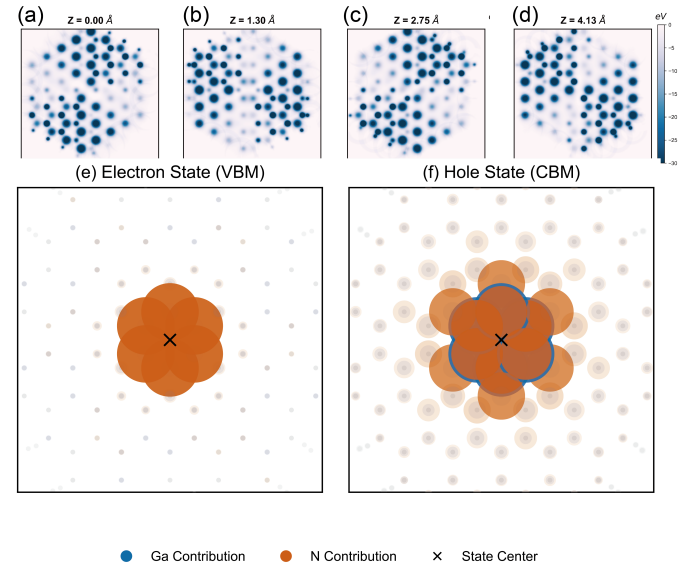


FIG. 7. Electrostatic potential distribution and orbital composition analysis of screw-dislocated GaN. (a)-(d) Cross-sectional maps of the electrostatic potential at different  $z$ -coordinates ( $z = 0.00, 1.30, 2.75$ , and  $4.13 \text{ \AA}$ ). (e)-(f) Orbital composition of state 3 and 4: The marker size represents the orbital weight, and colors represent atom types. Electron state is predominantly localized on Nitrogen atoms, while hole state is localized on Gallium atoms.

### D. Physical Interpretation

To elucidate the microscopic origin of the precipitous suppression of the radiative recombination rate, we identify a synergistic mechanism combining GaN's strong piezoelectric response with a local quantum confined effect induced by the screw dislocation [24–26].

Due to the large piezoelectric coefficients of GaN, the severe strain field of the screw dislocation generates a substantial internal electrostatic potential. As illustrated in Fig. 7(a)-(d), this potential exhibits a strong angular inhomogeneity within the  $xy$ -plane, characterized by distinct local minima and maxima. Crucially, due to the screw symmetry, this non-uniform potential distribution rotates along the  $z$ -axis. This spiraling potential landscape creates strong local electric fields along the  $z$ -direction, acting as a driving force for charge separation.

This internal field effectively transforms the dislocation core into a "quasi-quantum well" where charge carriers are spatially pulled apart. This spatial segregation is explicitly confirmed by the orbital composition analysis of the gap states near the Fermi level, as shown in Fig. 7(e) and (f). While both State 3 (below  $E_F$ ) and State 4 (above  $E_F$ ) are localized around the dislocation core, they exhibit distinct atomic origins: State 3 is pre-

dominantly distributed on Nitrogen (N) atoms, whereas State 4 is localized mainly on Gallium (Ga) atoms.

From a quantum-mechanical perspective, this spatial mismatch between the electron (Ga-dominated) and hole (N-dominated) wavefunctions drastically reduces the overlap integral. Consequently, the transition dipole matrix element  $\mathbf{d}_{fi} = -e \int \psi_f^*(\mathbf{r}) \mathbf{r} \psi_i(\mathbf{r}) d^3r$  vanishes because the integrand becomes negligible where the two wavefunctions do not co-locate. Since the spontaneous-emission rate scales as  $|\mathbf{d}_{fi}|^2$ , this separation leads directly to the observed reduction in radiative recombination by orders of magnitude.

### E. Implications for dislocation-related luminescence

Applying the selection rule (23) to the dislocation-localized states identified in the electronic-structure calculation immediately constrains both capture and emission pathways. For example, an optically allowed radiative recombination from a conduction-band state in block  $\mu_c$  to a dislocation state in block  $\mu_D$  requires  $\mu_D - \mu_c \equiv m \pmod{6}$ , and the emitted photon polarization then reflects the corresponding  $m$  channel.

In the specific case of GaN, our analysis indicates that the dominant radiative transitions originate from the dislocation-localized states 3 and 4. These transitions occur in the infrared spectral range and correspond to the  $\Delta\mu = 0$  channel. This implies that the emitted photons are linearly polarized parallel to the screw dislocation line. Consequently, the polarization anisotropy of this infrared luminescence offers a promising spectroscopic method to probe the spatial orientation and distribution of screw dislocations in bulk GaN.

## V. NONRADIATIVE RECOMBINATION

This section distills the essential results for phonon-mediated nonradiative recombination in the screw-dislocated GaN. The derivation follows the Born–Huang expansion and the projection formalism.

The nonadiabatic coupling driving transitions between electronic channels  $i \rightarrow f$  is given by the off-diagonal pieces of phonon Hamiltonian  $\hat{H}_{el}$ . Projected onto single-channel nuclear eigenstates  $\Psi_{i,\nu}(Q)$  (solutions of the diagonal channel nuclear equation), the phonon-mediated transition rate between channel eigenstates follows from Fermi's golden rule [27]:

$$W_{i\nu \rightarrow f\nu'} = \frac{2\pi}{\hbar} |M_{fi;\nu'\nu}|^2 \delta(\mathcal{E}_{f,\nu'} - \mathcal{E}_{i,\nu}), \quad (25)$$

where the matrix element is [28, 29]

$$M_{fi;\nu'\nu} = \int dQ \Psi_{f,\nu'}^*(Q) \hat{H}_{el} \Psi_{i,\nu}(Q). \quad (26)$$

For thermally populated initial nuclear states one obtains the total (channel-to-channel) rate

$$W_{i \rightarrow f}(T) = \sum_{\nu,\nu'} P_{i,\nu}(T) W_{i\nu \rightarrow f\nu'} \quad (27)$$

with Boltzmann weights  $P_{i,\nu}(T) = e^{-\beta\mathcal{E}_{i,\nu}}/Z_i(T)$ . The macroscopic nonradiative recombination rate follows by summing over defect concentrations and initial carrier populations as discussed earlier.

The final nonradiative recombination coefficient can be regarded as the superposition of the Huang–Rhys factor ( $S_k = \omega_k \Delta Q_k^2 / 2\hbar$ ) and electron-phonon coupling ( $W^{if}$ ) [30]. These two components are contributed by the phonons with different frequencies, which are shown in Fig. 8. It elucidates that while the Huang–Rhys factor involves contributions from phonons across the entire frequency spectrum, the low-frequency regime dominates the electron-phonon coupling. Consequently, the total non-radiative recombination coefficient is essentially determined by the low-frequency phonon modes.

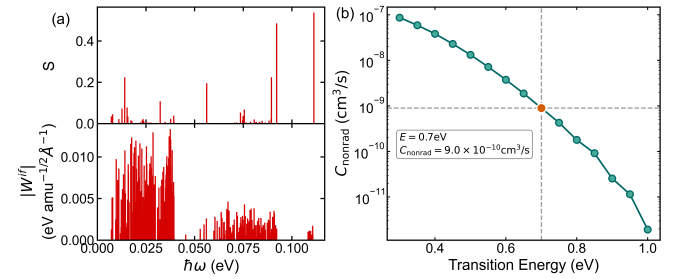


FIG. 8. The contribution of different phonon modes to the Huang–Rhys factor ( $S$ ), electron-phonon coupling matrix element ( $W^{if}$ ), and nonradiative capture coefficient ( $C_{\text{nonrad}}$ ).  $S$  involves contributions from phonons across the entire frequency spectrum and the low-frequency regime dominates the electron-phonon coupling.

From the phonon-mediated capture calculations we obtain the nonradiative recombination coefficient at energy gap  $\Delta E = 0.7$  eV and  $T = 300$  K is:

$$C_{\text{nonrad}} = 9.0 \times 10^{-10} \text{ cm}^3/\text{s}. \quad (28)$$

In contrast, the radiative coefficient is  $B_{\text{rad}} = 2.8 \times 10^{-14} \text{ cm}^3/\text{s}$ . Thus nonradiative processes dominate by many orders of magnitude under the considered conditions, implying that screw dislocations can severely quench photoluminescence and adversely affect the performance of GaN-based light-emitting devices.

Our calculated nonradiative recombination coefficient of the dislocation is comparable to the coefficient reported for the  $C_N$  defect in Ref. [31] ( $C_p = 3.1 \times 10^{-9} \text{ cm}^3/\text{s}$ ), and is consistent with the reduced recombination lifetimes observed in dislocation-rich GaN [8]. These agreements validate our finding that screw dislocations exhibit high nonradiative recombination rates.

## VI. CONCLUSION

In this paper, we have developed a compact and unified framework for analyzing electronic structure and radiative/nonradiative processes in crystals that host screw dislocations. Starting from the screw symmetry generator we constructed localized atomic orbital Bloch sums and discrete-group projectors that produce symmetry-adapted subspaces labeled by the screw representation index  $\mu$ . When the Hamiltonian commutes with the screw operator the projector construction yields an exact block decomposition  $\hat{H} = \bigoplus_{\mu} H_{\mu}(k)$  so that each block can be diagonalized independently to obtain symmetry-resolved bands  $\epsilon_{n,\mu}(k)$ . This approach avoids the inefficiencies of plane-wave supercell expansions for localized defect cores while preserving the full group-theoretic content of the problem.

Applying the method to GaN with a sixfold screw generator we proved a robust band-flow constraint ( $\Delta\mu = +2 \pmod{6}$ ) that enforces how bands from different  $\mu$ -blocks connect across the axial Brillouin-zone. The projector-based decomposition clarifies band assignments, enables polarization-resolved optical matrix-element analysis, and directly yields the selection rule  $\Delta\mu \equiv m \pmod{6}$  for electric-dipole transitions. These results give a transparent explanation for polarization-dependent selection channels and for how dislocation localized states couple to extended bands.

Using calculated Hamiltonians and optical matrix elements we computed radiative rates and the dielectric response resolved by  $\mu$ -channel. Our numerical results indicate a strong suppression (2–3 orders of magnitude) of radiative recombination in the presence of screw cores;

physically this is attributable to a piezoelectrically driven field that spatially separates electron and hole densities and therefore quenches the transition dipole. Finally, by streamlining the Born–Huang projection and derivative-coupling formalism, we evaluate the nonradiative recombination coefficient and find that it exceeds the radiative counterpart by several orders of magnitude, indicating that only a small fraction of excited carriers contributes to photon emission.

The symmetry-adapted block decomposition and the derived selection rules form a foundation for several follow-up studies: (i) generation of quantitative radiative and nonradiative lifetimes from converged DFT inputs and comparison with experiment; (ii) construction of reduced-order models for carrier transport along dislocation lines that incorporate  $\mu$ -resolved scattering channels; (iii) systematic exploration of other screw symmetries and their mathematically constrained coupling chains. We anticipate that the formal and computational tools presented here will aid interpretation of dislocation-related luminescence and carrier-loss mechanisms in wide-bandgap semiconductors and will generalize readily to other materials with screw structural motifs.

## ACKNOWLEDGMENTS

This work was supported by the National Natural Science Foundation of China (Grants No. 12188101, No. 12334005, No. 12404089, No. 1227408, No. 124B1003), National Key Research and Development Program of China (Grant No. 2024YFA1409800).

Y.X. and H.S. contributed equally to this work.

---

[1] W. Shockley and W. Read Jr, Statistics of the recombinations of holes and electrons, *Physical review* **87**, 835 (1952).

[2] F. Zhao, M. E. Turiansky, A. Alkauskas, and C. G. Van de Walle, Trap-assisted auger-meitner recombination from first principles, *Physical Review Letters* **131**, 056402 (2023).

[3] X. Zhang and S.-H. Wei, Origin of efficiency enhancement by lattice expansion in hybrid-perovskite solar cells, *Physical Review Letters* **128**, 136401 (2022).

[4] A. Stoneham, Non-radiative transitions in semiconductors, *Reports on Progress in Physics* **44**, 1251 (1981).

[5] Y. Liang, X. Cui, F. Li, C. Stampfl, S. P. Ringer, X. Yang, J. Huang, and R. Zheng, Origin of enhanced nonradiative carrier recombination induced by oxygen in hybrid sn perovskite, *The Journal of Physical Chemistry Letters* **14**, 2950 (2023).

[6] R. Valero, Á. Morales-García, and F. Illas, Estimating nonradiative excited-state lifetimes in photoactive semiconducting nanostructures, *The Journal of Physical Chemistry C* **128**, 2713 (2024).

[7] B. Wang, Y.-H. Zhou, S. Yuan, Y.-H. Lou, K.-L. Wang, Y. Xia, C.-H. Chen, J. Chen, Y.-R. Shi, Z.-K. Wang, and L.-W. Wang, Low-dimensional phase regulation to restrain non-radiative recombination for sky-blue perovskite leds with eqe exceeding 15%, *Angewandte Chemie* **135**, e202219255 (2023).

[8] Q. Gao, Z. Zheng, M. Fan, and L.-W. Wang, First principles calculations of carrier dynamics of screw dislocation, *npj Computational Materials* **11**, 45 (2025).

[9] L.-W. Wang, M. Ye, Y. Liu, and X. Jiang, Large scale plane-wave based density-functional theory simulations for electronic devices, in *2020 IEEE International Electron Devices Meeting (IEDM)* (IEEE, 2020) pp. 22–3.

[10] W. Jia, L.-W. Wang, and L. Lin, Parallel transport time-dependent density functional theory calculations with hybrid functional on summit, in *Proceedings of the International Conference for High Performance Computing, Networking, Storage and Analysis* (2019) pp. 1–23.

[11] M. Ye, X. Jiang, S.-S. Li, and L.-W. Wang, Large-scale first-principles quantum transport simulations using plane wave basis set on high performance computing platforms, *Computer Physics Communications* **260**, 107737 (2021).

[12] A. Sharma, *Symmetry-adapted density functional theory*, Ph.D. thesis, Georgia Institute of Technology (2022).

[13] A. Sharma and P. Suryanarayana, Real-space density functional theory adapted to cyclic and helical symmetry: application to torsional deformation of carbon nanotubes, *Physical Review B* **103**, 035101 (2021).

[14] M. Matsubara, J. Godet, L. Pizzagalli, and E. Bellotti, Properties of threading screw dislocation core in wurtzite gan studied by heyd-scuseria-ernzerhof hybrid functional, *Applied Physics Letters* **103** (2013).

[15] M. Matsubara, L. Pizzagalli, and E. Bellotti, Threading screw dislocations in gan by the heyd-scuseria-ernzerhof hybrid functional, *physica status solidi (c)* **11**, 521 (2014).

[16] M. Chen, G. Guo, and L. He, Systematically improvable optimized atomic basis sets for ab initio calculations, *Journal of Physics: Condensed Matter* **22**, 445501 (2010).

[17] P. Li, X. Liu, M. Chen, P. Lin, X. Ren, L. Lin, C. Yang, and L. He, Large-scale ab initio simulations based on systematically improvable atomic basis, *Computational Materials Science* **112**, 503 (2016).

[18] P. Lin, X. Ren, X. Liu, and L. He, Ab initio electronic structure calculations based on numerical atomic orbitals: Basic formalisms and recent progresses, *Wiley Interdisciplinary Reviews: Computational Molecular Science* **14**, e1687 (2024).

[19] P. Lin, X. Ren, and L. He, Efficient hybrid density functional calculations for large periodic systems using numerical atomic orbitals, *Journal of Chemical Theory and Computation* **17**, 222 (2020).

[20] P. Lin, X. Ren, and L. He, Accuracy of localized resolution of the identity in periodic hybrid functional calculations with numerical atomic orbitals, *The Journal of Physical Chemistry Letters* **11**, 3082 (2020).

[21] B. Monemar, Fundamental energy gap of gan from photoluminescence excitation spectra, *Physical Review B* **10**, 676 (1974).

[22] I. Vurgaftman and J. n. Meyer, Band parameters for nitrogen-containing semiconductors, *Journal of applied physics* **94**, 3675 (2003).

[23] S. Wang, M. Huang, Y.-N. Wu, W. Chu, J. Zhao, A. Walsh, X.-G. Gong, S.-H. Wei, and S. Chen, Effective lifetime of non-equilibrium carriers in semiconductors from non-adiabatic molecular dynamics simulations, *Nature Computational Science* **2**, 486 (2022).

[24] T. Takeuchi, S. Sota, M. Katsuragawa, M. Komori, H. Takeuchi, H. A. H. Amano, and I. A. I. Akasaki, Quantum-confined stark effect due to piezoelectric fields in gainn strained quantum wells, *Japanese Journal of Applied Physics* **36**, L382 (1997).

[25] J.-H. Ryou, P. D. Yoder, J. Liu, Z. Lochner, H. Kim, S. Choi, H. J. Kim, and R. D. Dupuis, Control of quantum-confined stark effect in ingan-based quantum wells, *IEEE Journal of Selected Topics in Quantum Electronics* **15**, 1080 (2009).

[26] S. Zhu, S. Lin, J. Li, Z. Yu, H. Cao, C. Yang, J. Li, and L. Zhao, Influence of quantum confined stark effect and carrier localization effect on modulation bandwidth for gan-based leds, *Applied Physics Letters* **111** (2017).

[27] K. Huang, Lattice relaxation and multiphonon transitions, *Contemporary Physics* **22**, 599 (1981).

[28] R. Pässler, Description of nonradiative multiphonon transitions in the static coupling scheme: I. foundations, *Czechoslovak Journal of Physics B* **24**, 322 (1974).

[29] R. Pässler, Description of nonradiative multiphonon transitions in the static coupling scheme ii. approximations, *Czechoslovak Journal of Physics B* **25**, 219 (1975).

[30] J. Zhou, S. Wang, M. Huang, X.-G. Gong, and S. Chen, Defect phonon renormalization during nonradiative multiphonon transitions in semiconductors, *Physical Review B* **111**, 115202 (2025).

[31] A. Alkauskas, Q. Yan, and C. G. Van de Walle, First-principles theory of nonradiative carrier capture via multiphonon emission, *Physical Review B* **90**, 075202 (2014).